Macedonian Journal of Chemistry and Chemical Engineering, Vol. **44**, No. 2, pp. 331–347 (2025)

MJCCA9 – 940

ISSN 1857-5552
e-ISSN 1857-5625

Received: March 17, 2025
Accepted: June 30, 2025

DOI: 10.20450/mjcce.2025.3103
Original scientific paper

PREPARATION, CHARACTERIZATION, ADSORPTION, AND ANTIBACTERIAL ASSESSMENTS OF SILANE-FUNCTIONALIZED ZEOLITES

Jelena Dimitrijević[1*], Jelena Petrović[1], Aleksandar Marinković[2], Jelena Dikić[3], Marija Koprivica[1], Marija Simić[1], Sanja Jevtić[2]

[1]*Institute for Technology of Nuclear and Other Mineral Raw Materials, 86 Franchet d'Esperey St., 11000 Belgrade, Serbia*
[2]*Faculty of Technology and Metallurgy, University of Belgrade, Karnegijeva 4, 11000 Belgrade, Serbia*
[3]*Innovation Centre of the Faculty of Technology and Metallurgy, University of Belgrade, Karnegijeva 4, 11000 Belgrade, Serbia*

j.dimitrijevic@itnms.ac.rs

In this work, the preparation and comparative analysis of two adsorbents based on silane-modified natural and synthetic zeolite for adsorbing silver ions from aqueous solutions and the assessment of the possibility of their application as antibacterial agents against two strains of bacteria was conducted. (3-Aminopropyl) triethoxysilane (APTES) was employed for modification, the presence of which in the obtained samples was verified by thermal and Brunauer-Emmett-Teller (BET) analysis, as well as infrared spectroscopy. Kinetic analysis indicated that the silver adsorption process followed the Lagergren pseudo-second-order model, while the data fit best with the Freundlich isotherm, indicating multilayer adsorption on the heterogeneous surface. The maximum adsorption capacities for silver ions were measured at 89.49 mg/g for natural and 61.19 mg/g for synthetic beta zeolite. The higher silver binding capacity was observed in natural zeolite, which led to the conclusion that the key role in silver binding was played by exchangeable cations in the structure of this starting material and that the dominant mechanism was ion exchange. Both materials exhibited good antibacterial properties against Gram-negative *Escherichia coli* and the Gram-positive *Staphylococcus aureus*. These findings demonstrated the potential of APTES-modified zeolites as efficient adsorbents for silver ion removal and as antibacterial agents, paving the way for applications in water purification and antimicrobial technologies.

Keywords: natural zeolite; beta zeolite; modified zeolite; APTES; silver ion; antibacterial activity

ПОДГОТОВКА, КАРАКТЕРИЗАЦИЈА, АТСОРПЦИЈА И ПРОЦЕНКА НА АНТИМИКРОБНАТА АКТИВНОСТ НА ЗЕОЛИТИ ФУНКЦИОНАЛИЗИРАНИ СО СИЛАН

Во оваа студија е извршена подготовка и споредбена анализа на два атсорбента базирани на природен и синтетички зеолит модифициран со силан за атсорпција на сребрени јони од водни раствори, како и проценка на можноста за нивна примена како антимикробни средства против два соја бактерии. За модификација беше користен (3-аминопропил)триетоксисилан (APTES), чие присуство во добиените примероци беше потврдено со термална анализа, Brunauer-Emmett-Teller – ова (BET) анализа и инфрацрвена спектроскопија. Кинетичката анализа укажа дека процесот на атсорпција на сребро се одвива според псевдо-втор ред на Lagergren, додека податоците најдобро се вклопуваат со изотерма на Freundlich, што укажува на повеќеслојна атсорпција на хетерогена површина. Максималните капацитети за атсорпција на сребрени јони изнесуваа 89,49 mg/g за природниот и 61,19 mg/g за синтетичкиот бета-зеолит. Поголемата способност за врзување на сребро беше забележана кај природниот зеолит, што доведе до заклучок дека клучна улога во врзувањето на сребро играат изменливите катјони во структурата на овој почетен материјал и дека доминантен механизам е јонската измена. И двата материјала покажаа добри антимикробни

својства против Грам-негативната *Escherichia coli* и Грам-позитивниот *Staphylococcus aureus*. Овие наоди ја потврдуваат можноста за примена на зеолити модифицирани со APTES како ефикасни атсорбенти за отстранување на сребрени јони и како антимикробни средства, отворајќи пат за нивна употреба за прочистување на вода и во антимикробни технологии.

Клучни зборови: природен зеолит; бета зеолит; модифициран зеолит; APTES; сребрен јон; антибактериска активност

1. INTRODUCTION

Zeolites, depending on their origin, exhibit different structural and functional properties that determine their effectiveness in various types of applications. Clinoptilolite, the most abundant natural zeolite, has a limited pore size and a relatively small specific surface area.[1–3] However, natural zeolites have a large number of exchangeable cations in their structure due to the low silicon content, which make them efficient in adsorption processes.[4–7] In contrast, synthetic beta zeolite has a significantly larger pore volume, a high-silicate open three-dimensional network of interconnected channels, and a large specific surface area. These improvements makes beta zeolite adaptable for achieving functionality and binding large organic molecules, both on the surface and within the channels and cavities.[7–9]

Improving the performance of zeolites often involves surface modification. Previous studies have shown that natural zeolites have the highest affinity for binding ions of lead, copper, and zinc, followed by cadmium and nickel.[10] However, the practical application of natural zeolite remains limited by its lower adsorption capacity and selectivity. In recent years, researchers have modified natural zeolites with compounds containing organofunctional groups to increase the adsorption capacity and selectivity. Functionalization of zeolites with silanes, such as (3-aminopropyl)triethoxysilane (APTES), introduces amino groups that increase hydrophobicity, mechanical stability, and ion exchange capacity.[11,12] It has been shown that APTES-modified zeolites can immobilize metal ions such as silver, zinc, or copper,[13] thereby producing materials with antibacterial activity that have potential applications in biomedicine.[14–17]

Beta zeolite is one of the most commonly used synthetic zeolites. The large specific surface area is attributed to the existence of channels in the structure formed by the interconnection of 12-membered rings with an aperture diameter of 7.7 Å.[18] Beta zeolite exhibits superior properties in the adsorption of large volatile organic compounds and carbon dioxide, which is mainly attributed to its large total pore volume and specific surface area, as well as excellent hydrophobicity.[19] It has also been shown to be an effective adsorbent for drugs such as the commonly used ketoprofen, hydrochlorothiazide, and atenolol from dilute aqueous solutions.[20] Beta zeolite, synthesized without organic structure-directing agents, and saturated with silver ions, has demonstrated surprisingly good antibacterial activity in just one hour, killing all *E. coli* bacteria present in the water medium.[21]

Considering that silver ions can damage bacterial cell membranes and interfere with enzymatic processes,[22,23] the aim of this work was to compare the preparation of two adsorbents based on APTES-modified natural zeolite (ANZ) and synthetic beta zeolite (ABZ) and their application for the adsorption of silver ions. Starting from the assumption that in natural zeolite the dominant binding mechanism is ion exchange, while in beta zeolite the binding occurred exclusively through APTES groups, the contribution of organofunctional groups to the silver adsorption capacity was compared in the work. Based on the study of the antibacterial activity of Ag-saturated zeolites, their potential application in wastewater treatment and medicine to reduce microbial contamination is assessed.

2. EXPERIMENTAL SECTION

2.1. *Chemicals*

All chemicals and reagents used in this investigation were of analytical grade. The primary stock silver solution (1000 mg/l) was prepared by dissolving a precise quantity of silver nitrate (Sigma Aldrich, Germany) in ultra-distilled water. The working solution concentrations were prepared by appropriately diluting the primary stock solutions. (3-Aminopropyl)triethoxysilane (APTES, 99% purity, Acros Organics) was used as the zeolite modifier. The beta zeolite (BZ) used in this study was acquired from Sigma Aldrich (particle size < 20 μm).

2.2. *Zeolite preparation*

For this research, natural zeolite (NZ) from the Zlatokop deposit near Vranjska Banja was used. To obtain the optimal sample for the prepara-

tion of the adsorbent, the zeolite was first ground, after which separation was carried out using a sieve shaker (CISA, BA200N). The separation process was conducted in four series, each lasting 10 minutes, with the amplitude set to 2.0. A sieve was used to isolate the zeolite fraction with a grain size of –125 μm.

2.3. *Aminosilane modification*

Encouraged by previous publications,[24,25] NZ and BZ modification was performed using APTES, with certain procedural changes. A mass of 3.0 g of zeolite and introduced 1.0 g of APTES (zeolite:APTES ratio of 3:1) were suspended in 50 ml of a mixture of toluene and ethanol solution (70:30). The suspension was heated in an oil bath for 9 hours at a controlled temperature (70 °C) under reflux in an inert nitrogen atmosphere. The modification was carried out under these conditions to suppress hydrolysis and oxidative degradation of APTES, ensuring efficient and reproducible functionalization of the zeolite surface.

Upon completion of the modification step, the zeolite was centrifuged, separated, and washed three times with 15 ml of 99 % ethanol to remove unbound materials. After that, the material was dried at 50 °C for 12 hours to ensure the stability and consistency of the sample. This process ensured the optimal functionalization of zeolite with APTES, which contributed to the improvement of the adsorption characteristics of the material.

Beta zeolite was also modified according to the same procedure. The samples were labeled as ANZ and ABZ after modification.

2.4. *Characterization of the obtained material*

X-ray powder diffraction (XRPD) was used to identify and analyze the phase composition of the samples, as well as to determine the degree of crystallinity of the adsorbent. The samples were examined using a Philips X-ray diffractometer, model PW1710, equipped with a high-quality curved graphite monochromator in conjunction with a scintillation counter. Measurements of the intensity of diffracted CuKα X-ray radiation (λ=1.54178 Å) were carried out at room temperature under precisely defined parameters. The X-ray tube operated at 40 kV and 30 mA, while the apertures for directing the primary and diffracted beams were adjusted to 1° and 0.1 mm, respectively, ensuring optimal measurement precision and stability.

Thermal properties were characterized by Thermogravimetric and Derivative Thermogravimetric analysis (TG/DTG) using an SDT Q600 instrument (TA Instruments). The samples were heated in a stream of synthetic air at a constant flow rate of 100 ml/min and a heating rate of 10 °C/min, up to a maximum temperature of 800 °C. This method provided a detailed examination of changes in sample mass as a function of temperature, offering deeper insight into the thermal properties of the material.

For Fourier transform infrared (FTIR) spectroscopy analysis, a Nicolet iS10 spectrometer manufactured by Thermo Scientific was employed. Spectra were recorded in the range of 4000 to 450 cm^{-1} using the pressed KBr tablets method.

Scanning electron microscopy (SEM) was utilized to investigate the morphology of the samples and to analyze the size of single crystals within crystalline aggregates. A JEOL JSM-6610LV electron microscope was used at an operating voltage of 20 keV. Prior to analysis, the samples were dried overnight at 105 °C, after which a thin layer of gold was applied to their surface by sputter coating to improve conductivity during SEM imaging.

Analysis of specific surface area and pore distribution was performed via nitrogen adsorption testing at –196 °C using a Micromeritics ASAP 2020 analyzer. Before measurement, the samples were degassed overnight at either 100 °C (for organic/biopolymer components sensitive to higher temperatures) or 150 °C (for inorganic and thermally stable hybrid samples). The specific surface area of the powder materials was determined based on their gas adsorption capacity using the Brunauer-Emmett-Teller (BET) method, while the volume and surface area of the mesopores were measured using the Barrett-Joyner-Halenda (BJH) methodology.

2.5. *Back titration of amino groups*

To determine the amino group content in functionalized materials, back titration was used as a precise and reliable method.[26] Approximately 10 mg of the functionalized adsorbent was accurately weighed and placed into a clean Erlenmeyer flask. To the flask, 10 ml of 0.01 mol/l hydrochloric (HCl) acid was added, allowing the acid to react with the amino groups present on the material's surface. The mixture was subjected to ultrasonic agitation for 15 minutes to ensure thorough interaction between the acid and the surface functional groups.

After the reaction, the solid material was separated from the liquid phase through vacuum filtration, and the filtrate – containing the unreacted HCl – was collected for subsequent analysis.

The amount of unreacted acid was determined by titration with a 0.01 mol/l potassium hydroxide (KOH) solution. A few drops of methyl orange were used as an indicator, and the titration was considered complete when the solution changed color from red to yellow, indicating neutralization.

The volume of the KOH used during titration was recorded and used to calculate the number of moles of HCl that reacted with the amino groups (predominantly primary $–NH_2$, with possible contributions from secondary –NHR and tertiary $–NR_2$ functionalities). This calculation was done by subtracting the amount of unreacted HCl (as determined by titration) from the initial amount of HCl added. The amino group content were then expressed in mmol per gram of the material, normalized to the weight of the sample.[27]

2.6. *Adsorption experiments*

For the adsorption of silver ions, solutions with different initial concentrations (50, 100, 150, 200, 300, and 400 mg/l) were prepared. To minimize light exposure, the vessels were wrapped in aluminum foil. Adsorption experiments were conducted at pH 5, using 100 ml Erlenmeyer flasks, each containing 0.5 g of adsorbent in 50 ml of solution. The flasks were placed on a Heidolph Unimak 1010 orbital shaker at 25 °C, with a solid-liquid ratio of 1:100 (g/ml) and a mixing time of 15 to 1440 minutes.

For kinetic experiments, silver ion solutions with initial concentrations of 200 and 300 mg/l (referred to as Ag 200 and Ag 300) were used. These concentrations were chosen to evaluate the time-dependent adsorption performance of ANZ and ABZ. After mixing, the suspensions were filtered through medium-porosity filter paper using a water vacuum pump, and the filtrates were analyzed by atomic absorption spectroscopy (AAS) using a PerkinElmer 900T instrument.

All tests were performed in triplicate, and the average results were reported. The amount of adsorbed silver ions was calculated using the following equation:

$$q_e = \frac{(c_i - c_e)V}{m} \quad (1)$$

where q_e represents the amount of adsorbed silver on APTES-modified zeolites (mg/g), c_i and c_e are the initial and equilibrium metal concentrations (mg/l), V is the volume of the metal solution (l), and m is the mass of ANZ and/or ABZ (g). Zeolite samples enriched with Ag^+ ions (Ag-ANZ and Ag-ABZ) were subsequently dried at 50 °C overnight following filtration.

2.7. *Determination of cation exchange capacity*

The cation exchange capacity (CEC) was determined by suspending a 1.0 g sample in 100 ml of 1.0 mol/l ammonium acetate solution. The suspension was stirred in a water bath at 105 rpm and 25 °C for 24 hours. After mixing, the suspension was separated by filtration through medium-porosity filter paper using a vacuum pump.

The concentrations of Na^+, Ca^{2+}, K^+, and Mg^{2+} in the filtrate were measured using AAS. The CEC value was calculated by summing the concentrations of alkali and alkaline earth metal ions present in the solution and was expressed in mmol M^+/100 g of sample.

2.8. *Examination of antibacterial activity*

The antibacterial activity of samples Ag-ANZ, Ag-ABZ, and pure APTES was tested against two bacterial strains: Gram-negative *Escherichia coli* DSM 498 and Gram-positive *Staphylococcus aureus* ATCC 25923. The method used to evaluate the antibacterial effect of zeolite was a modified disk diffusion method in physiological solution (0.85 % NaCl), known as the Kirby-Bauer method.[28]

Bacterial cultures were grown on solid nutrient media for 16 hours at 37 °C to reach the logarithmic growth phase. Fresh bacterial biomass was suspended in 9.0 cm^3 of saline and homogenized using a vortex mixer for 3 minutes prior to testing.

All samples were sterilized in an autoclave at 121 °C for 20 minutes, except for the silver-containing samples, which were sterilized at 70 °C for 2 hours due to silver's thermal sensitivity. After sterilization, zeolite suspensions were prepared in solution at concentrations of 5, 10, and 20 mg/cm^3.

Bacterial strains were seeded onto solid nutrient agars, and 10 µl of each suspension at varying concentrations were dropped onto the agar surface. After incubation for 24 hours at 37 °C, the zone of inhibition was measured to assess the antibacterial activity of the samples.

3. RESULTS AND DISCUSSION

3.1. *Adsorbent characterizations*

The X-ray powder diffraction (XRPD) method was used to identify the crystalline phases present in the natural (NZ) and beta zeolite (BZ) samples analyzed in this study. The diffractogram

of NZ powder is shown in Figure 1, which shows characteristic peaks attributed to clinoptilolite at 2Θ positions of 9.7°, 12.8°, 17.2°, 19°, 22.2°, and 29.9°. In addition, peaks originating from quartz (2Θ = 20.9°, 26.6°, and 36.5°) and feldspar (2Θ = 27.1°) were observed, indicating the presence of these mineral impurities in the zeolitic tuff from the Zlatokop deposit.

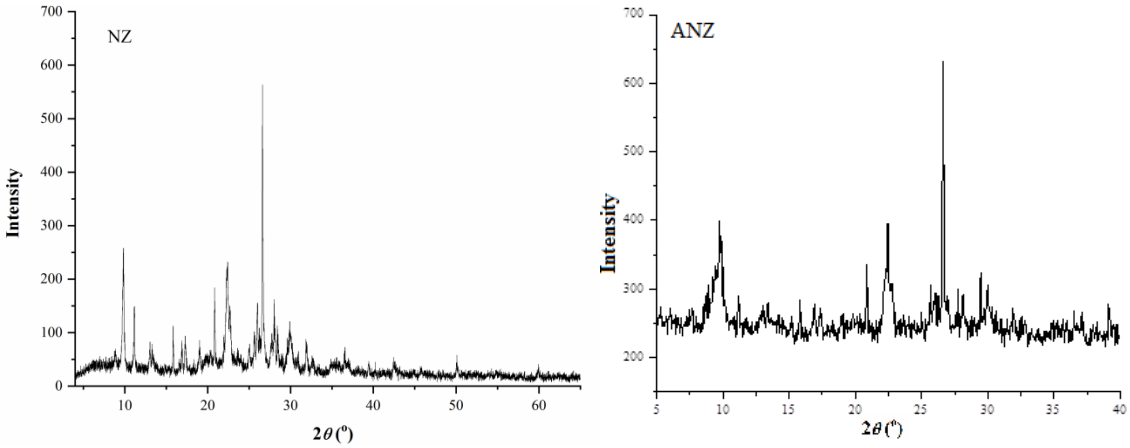

Fig. 1. Diffractograms of NZ and ANZ

Through detailed analysis, it was determined that NZ contained 72 wt.% clinoptilolite, with the main impurities being feldspar (14 wt.%), quartz (12 wt.%), and clay (2 wt.%). After APTES modification (ANZ sample), all peaks were observed with lower intensity, indicating that the structure was preserved and only weak amorphization occurred due to acid exposure (Fig. 1).[29,30]

Furthermore, XRPD analysis of the BZ (Fig. 2) revealed a diffractogram corresponding to the crystalline structure of the beta zeolite, in agreement with the Atlas of Zeolite Structures[31] issued by the World Zeolite Association. XRPD analysis after silanization (Fig. 2, sample ABZ) showed that the modification led to partial amorphization of the sample, although the overall structure remained intact.[32]

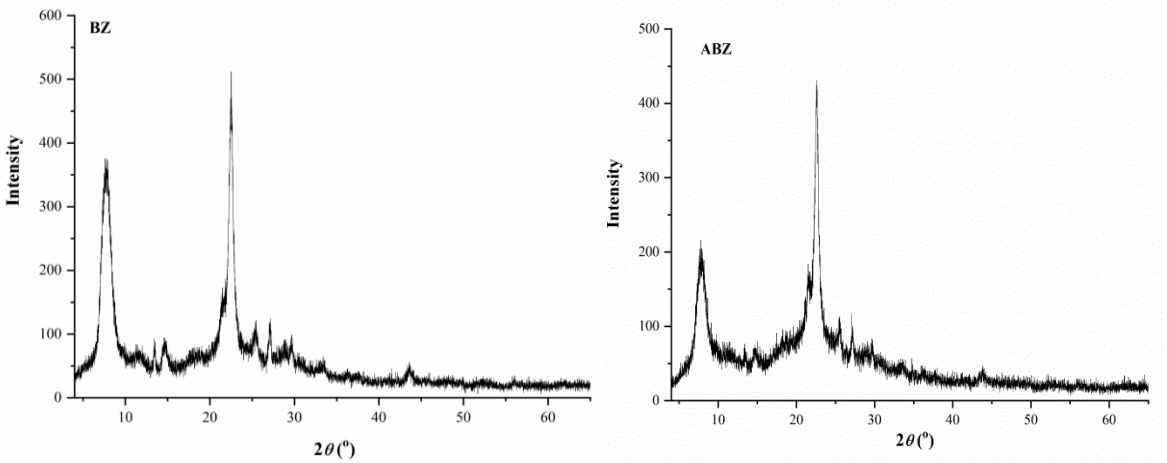

Fig. 2. Diffractograms of BZ and ABZ

The thermal properties were examined using TG/DTG analysis to understand how the samples responded to high temperatures and to determine whether aminosilane had bonded to the zeolite surface.

The thermogravimetric (TG) and differential thermogravimetric (DTG) curves for NZ and ANZ are presented in Fig. 3. The samples were heated from 25 to 800 °C. The NZ sample showed a total mass loss of 12.3 wt.%, primarily due to dehydration. In contrast, the ANZ sample exhibited a mass loss of 15.1 wt.%, which was attributed to both dehydration and decomposition of the organic components (Fig. 3a).[33]

The difference in mass loss between the unmodified and APTES-modified zeolite indicated the presence of grafted organic groups on the zeolite surface. Specifically, the NZ sample had a total mass loss 2.8 wt.% lower than that of ANZ, suggesting that approximately 2.8 wt.% of the added mass corresponded to covalently bonded aminopropyl moieties introduced via APTES modification.

This result is consistent with previously reported data, where a mass loss of 3.9 wt.% in the 200 – 800 °C range was attributed to the thermal decomposition of propyl chains in silane-functionalized materials.[34] The agreement between the observed mass difference and the literature-reported decomposition profile further supports the successful surface functionalization of the zeolite with aminopropyl groups.

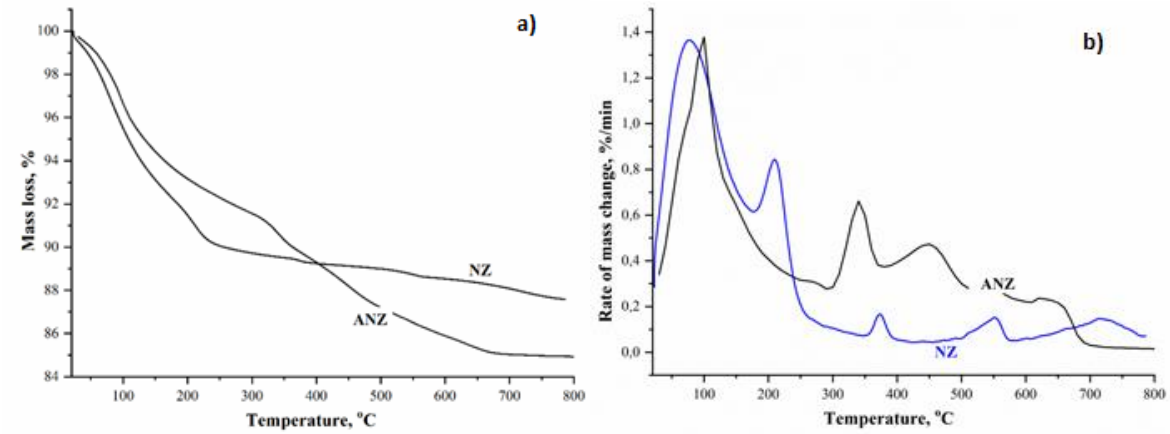

Fig. 3. a) TG curves of NZ and ANZ and **b)** DTG curves of NZ and ANZ

The DTG curve for the NZ sample (Fig. 3b) showed maxima at 76, 209, 373, 551, and 716 °C, which were attributed to the loss of surface-bound water and water incorporated within the zeolite framework.[35] In contrast, the DTG profile of the ANZ sample revealed three distinct peaks. The first, observed near 100 °C, corresponded to the release of physically adsorbed water and water associated with hydrated cations in the zeolite structure. The subsequent peaks at 342 °C and 447 °C were attributed to the stepwise thermal decomposition of the grafted APTES moiety. These features indicated the presence of the organic modifier on the zeolite surface and confirmed that APTES underwent degradation in two successive stages.

Thermal analysis results shown in Figure 4 (TG and DTG curves) provided insight into the differences in thermal behavior between the unmodified (BZ) and APTES-modified (ABZ) synthetic zeolite samples. The total weight loss recorded for BZ was 11.5 wt.%, primarily due to the removal of physically adsorbed water and surface-bound hydroxyl groups through dehydration. In contrast, the ABZ sample exhibited a significantly higher total mass loss of 24.2 wt.%, reflecting the combined effects of dehydration, dehydroxylation, and thermal decomposition of grafted organic functionalities introduced during silanization (Fig. 4a).

The observed difference in mass loss (12.7 wt.%) between BZ and ABZ was attributed to the incorporation of aminopropyl groups from the APTES modifier. This increase suggests not only surface functionalization but also substantial penetration of the organosilane into the internal pore network of the beta zeolite. The enhanced thermal response of ABZ indicates a more extensive and spatially distributed immobilization of organic matter, supporting the successful functionalization of the material at both surface and intracrystalline levels.

The DTG curve for the BZ (Fig. 4b) showed maxima at 76 and 206 °C, which were attributed to the loss of surface-bound and structural water.[36] On the DTG curve of the ABZ sample, multiple peaks were observed. The low-temperature peaks below 100 °C corresponded to the loss of physisorbed and water associated with hydration cations.

In addition, three distinct peaks at 265, 331, and 378 °C were attributed to the stepwise thermal decomposition of the grafted APTES molecules. The appearance of these three peaks, along with a larger area under the curves, indicates the presence of a greater amount of organic material bound to the zeolite surface compared to NZ.[37]

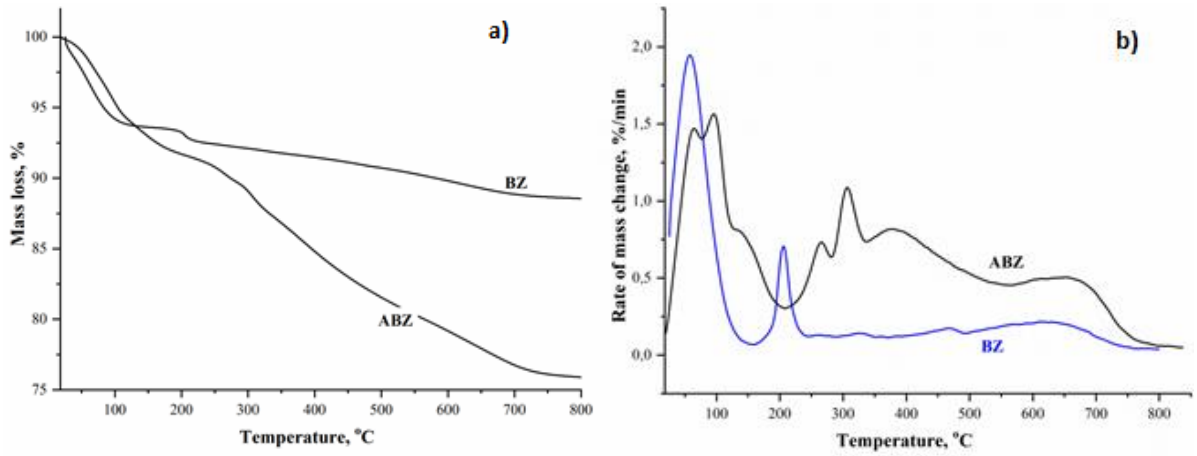

Fig. 4. a) TG curves of BZ and ABZ and **b)** DTG curves of BZ and ABZ

The FTIR spectrum of all samples (Figs. 5a and 5b) showed a pronounced band in the range of 3400 – 3500 cm^{-1}, attributed to the stretching vibrations of –OH groups. A peak at 1634 cm^{-1} was observed, corresponding to –OH bending vibrations associated with cations located within the zeolite channels.[38,39]

The characteristic band at 1060 – 1075 cm^{-1} corresponded to asymmetric vibrations of internal Si–O and Al–O bonds in SiO_4 and AlO_4 tetrahedral groups, while the band at 796 cm^{-1} was attributed to the stretching vibrations of O–Si–O and O–Al–O groups in the zeolite structure.

In addition to the typical absorption bands of –OH, Si–O, and Al–O groups, new bands appeared in the spectra of silane-modified zeolites, indicating successful incorporation of APTES onto the zeolite surface. Peaks at 2958, 2923, and 2852 cm^{-1} were associated with –C–H stretching vibrations from aliphatic methylene groups.

Symmetric and asymmetric bending vibrations of –C–H groups in the $–CH_3$ plane were expected in the range of 1300 – 1500 cm^{-1}, along with bands corresponding to in-plane vibrations of –N–H and –C–N bonds, which overlapped with –C–H vibrations. A broad peak in the range of 3300 – 3600 cm^{-1} originated from $–NH_2$ stretching vibrations of the amino group, overlapping with –OH stretching vibrations.[39,40]

Scanning electron microscopy (SEM) was used to analyze the morphology of natural and synthetic beta zeolite samples, allowing examination of the structural characteristics of both materials (Fig. 6). Based on the scanned images, it was concluded that NZ formed aggregates through the adhesion of plate-like crystals approximately 25 μm in size, while BZ exhibited a granular structure with grains ranging from 1 to 2 μm. This observation is consistent with the known morphological characteristics of zeolites, which are typically described as granular materials.[28,35]

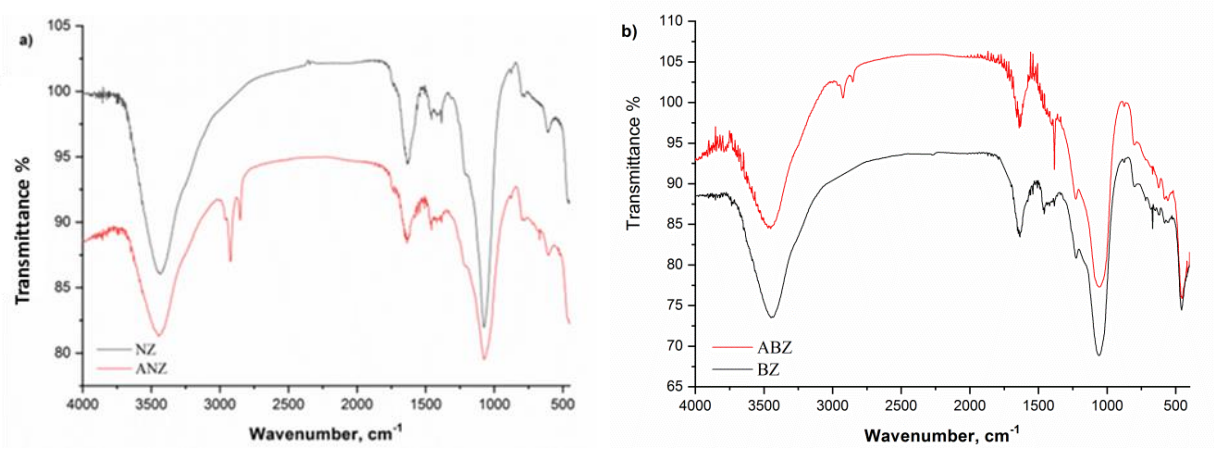

Fig. 5. FT-IR spectra of (a) NZ and ANZ and (b) BZ and ABZ

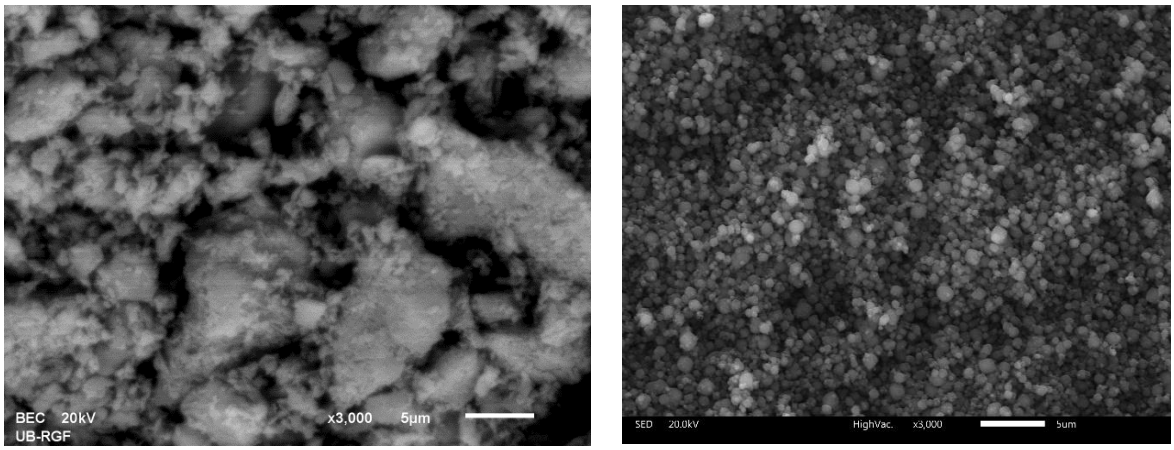

Fig. 6. SEM images of NZ and BZ

The results obtained from BET analysis are shown in Table 1. The specific surface area was measured for both zeolite samples before and after silane modification. Since APTES molecules are larger than the channels and cavities within the NZ structure, their binding occurred primarily on the external surface of the zeolite, which resulted in a reduction in specific surface area.[30,32]

A significant decrease in specific surface area was also observed in BZ, which suggests a greater amount of organic components present both on the surface and within the lattice cavities. In addition, a decrease in pore volume and average pore diameter was noted, which correlates with the reduction in surface area.[41]

T a b l e 1

Determined structural properties of base and fabricated materials

Sample	Specific surface area (m^2/g)	$V_{tot}(cm^3/g)$	$V_{meso}(cm^3/g)$
NZ	31.29	0.03	0.04
ANZ	6.3	0.13	0.13
BZ	587.52	1.13	0.41
ABZ	75.14	0.38	1.14

The results of the back titration revealed significant differences in amino group content between the two functionalized adsorbents, ANZ and ABZ, reflecting their surface modification efficiencies. ABZ showed a higher amino group content of 0.40 mmol/g, compared to 0.30 mmol/g for ANZ. These values confirmed the successful functionalization of both materials, while highlighting the enhanced modification efficiency of ABZ.

The higher amino group content in ABZ was attributed to the structural properties of BZ. The large pore size and three-dimensional interconnected channels of BZ provided more accessible surface sites for functionalization. Additionally, its greater thermal and chemical stability during modification ensured efficient grafting of aminosilanes, resulting in a denser distribution of amino groups.

However, not all amino groups in ABZ were equally accessible due to its complex pore network, as previously reported by Breck[42] and Mintova et al.[43] In contrast, ANZ possessed a smaller and less complex structure with smaller pore size, which limited the number of reactive sites available for modifications but enhanced the accessibility of functional groups.

This structure suggests a trade-off between functional group density and accessibility, as confirmed by Cundy et al.[44] These findings aligned with the TGA/DTG results, which confirmed a higher degree of APTES incorporation in ABZ, as evidenced by both greater mass loss and a significant reduction in surface area.

3.2. *Batch adsorption tests*

Previous adsorption studies revealed a significant improvement in adsorption capacity following the modification of NZ and BZ.[45] As shown, from a solution with an initial concentration of 100 mg Ag/l, the adsorption capacity of NZ increased from 25.3 to 58.49 mg/g, while that of BZ increased from 24.3 to 51.19 mg/g after APTES modification. These results demonstrate a substantial enhancement in the performance of the modified zeolites. Accordingly, in this study, adsorption kinetics were investigated to evaluate the efficiency of ANZ and ABZ as adsorbents of silver ions in aqueous solutions.

In addition to the structural changes caused by the modification, the influence of ion exchange on

the adsorption efficiency was also examined. A comparative analysis between modified and unmodified zeolites (ANZ and NZ) indicated that modification significantly enhanced the ability to bind silver ions through both ion exchange and surface complexation mechanisms. The results for exchangeable calcium, magnesium, sodium, and potassium, shown in Table 2, support this conclusion.

T a b l e 2

Exchangeable cations compared to silver

Adsorbent	Ag^+	Ca^{2+}	Mg^{2+}	Na^+	K^+
			meq M^+/100 g		
NZ	23.74	11.72	3.94	4.57	3.81
ANZ	54.65	13.84	4.48	5.82	4.92
BZ	22.71	3.43	3.21	10.64	5.51
ABZ	47.84	3.98	4.15	13.54	6.82

3.3. *Proposed mechanisms of Ag^+ binding*

For both NZ and BZ samples, the primary mechanism of Ag^+ binding was ion exchange, in which silver ions replaced exchangeable cations (Na^+, Ca^{2+}, K^+, Mg^{2+}) originally present in the zeolite framework:

$$\text{Zeolite–Na}^+ + \text{Ag}^+ \rightarrow \text{Zeolite–Ag}^+ + \text{Na}^+$$

This process was more pronounced in the NZ sample due to its higher content of exchangeable cations inherent to the natural zeolite structure. The observed decrease in the concentrations of these cations following Ag^+ uptake (Table 2) supports the predominance of this mechanism.

In the case of APTES-functionalized zeolites (ANZ and ABZ), Ag^+ binding occurred via a dual mechanism. In addition to ion exchange, the amino groups ($–NH_2$) introduced through surface grafting of APTES enabled the formation of coordination complexes with silver ions:

$$\text{Zeolite–NH}_2 + \text{Ag}^+ \rightarrow \text{Zeolite–NH}_2\cdots\text{Ag}^+$$

This additional complexation pathway significantly enhanced Ag^+ uptake in ANZ and ABZ, as demonstrated by both the increased adsorption capacities and the concurrent reduction of exchangeable cation concentrations. The synergistic contribution of ion exchange and surface complexation with amino functionalities explains the improved binding performance of the modified zeolites.

3.4. *Effect of contact time and kinetics studies*

As can be seen from Figure 7, the adsorption process was very fast – approximately 50 % of Ag^+ ions were removed from solutions of both concentrations within the first 15 minutes by ABZ (28 and 34 mg Ag/l). This phenomenon was attributed to the fast interaction of silver ions with available active sites on the adsorbent surface.[46,47]

Following this initial phase, a modest increase in adsorption capacity was observed until the system reached equilibrium. The adsorption capacity of ANZ was measured at 56.7 and 71.4 mg Ag/g for initial concentrations of 200 and 300 mg Ag/l, respectively, with equilibrium achieved after 240 minutes. In comparison, ABZ reached equilibrium faster – after 120 minutes – with adsorption capacities of 51.1 and 64.9 mg Ag/g at the same initial concentrations (Fig. 7).

APTES-modified zeolite binds silver ions more efficiently than unmodified samples, despite partial pore blockage caused by silane attachment to the zeolite surface. This efficiency is due to the introduction of amino groups ($–NH_2$), which serve as additional active sites.[48] These groups exhibit strong coordination interaction with the silver ions, enhancing adsorption performance. Although pore accessibility is slightly reduced, the additional functionalities compensate by creating new binding sites on the outer surface and at the pore entrances. In addition to ion exchange, selective chemisorption also occurs, providing stronger interactions and higher adsorption capacity.[10]

ANZ demonstrated greater efficiency in silver ion binding compared to ABZ. Although NZ possessed a smaller and more complex pore network, its lower Si/Al molar ratio resulted in a higher number of exchangeable cations available for interaction with silver ions. In contrast, BZ featured a more open structure with larger pores, which allowed organic molecules to occupy lattice channels, hindering silver ion diffusion and access to active binding sites.[49]

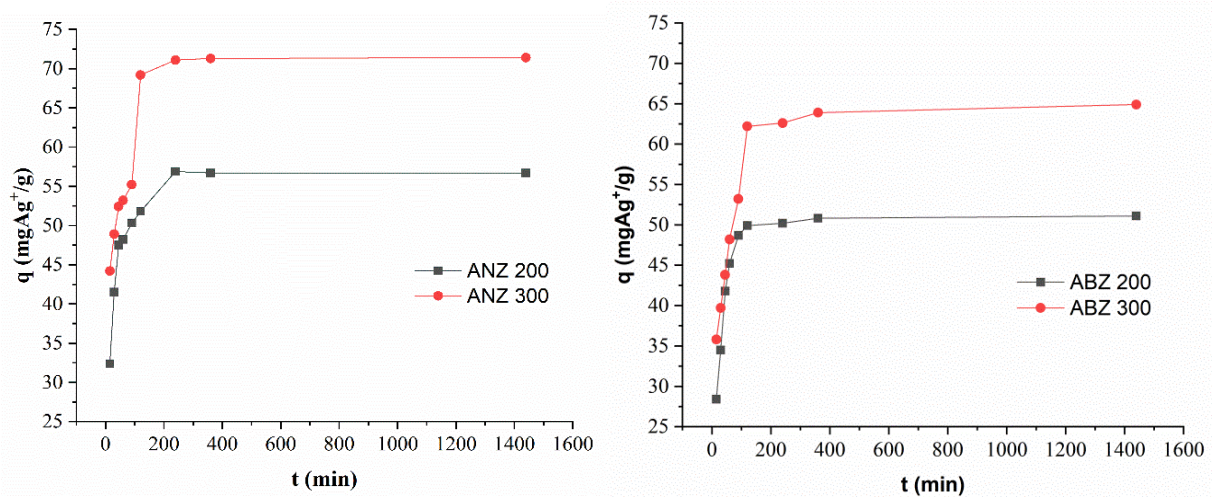

Fig. 7. The effect of contact time during Ag^+ ion removal using ANZ and ABZ, at different concentrations (200 and 300 mg Ag/l)

The kinetic investigation of adsorption provided valuable insights into the binding mechanisms of silver ions, the rate of sorption, and the potential degree of rate limitation. To clarify these aspects, various kinetic models – including the pseudo-first-order,[50] pseudo-second-order,[51] and Weber-Morris intraparticle diffusion models[52] – were applied to the experimental data. The mathematical equations of these models are shown below:

Pseudo-first-order rate equation:

$$\frac{1}{q_t} = \left(\frac{k_1}{q_{eq}}\right)\left(\frac{1}{t}\right) + \left(\frac{1}{q_{eq}}\right) \quad (2)$$

Pseudo-second-order rate equation:

$$\frac{t}{q_t} = \left(\frac{1}{k_2 q_{eq}^2}\right) + \left(\frac{1}{q_{eq}}\right)t \quad (3)$$

Intraparticle diffusion model equation:

$$q_t = K_{id}t^{0.5} + C \quad (4)$$

where q_{eq} and q_t denote the amount of silver adsorbed (mg/g) at equilibrium and at time t, respectively. The parameters k_1(1/min), k_2 (g/mg·min), and K_{id} (mg/g·$min^{1/2}$) represent the pseudo-first-order, pseudo-second-order, and intraparticle diffusion rate constants, respectively. The constant C represents the boundary layer effect.

The adsorption profiles based on the pseudo-second-order kinetic model and intraparticle diffusion for both modified zeolites are depicted in Figure 8. The corresponding calculated parameters are summarized in Tables 3 and 4. Analysis of the results presented in these tables revealed that the correlation coefficient values (R^2) for silver ions at both concentrations on ANZ and ABZ were notably higher and closer to 1 for the pseudo-second-order kinetic model. These findings indicated that the removal kinetics of silver ions on the surfaces of ABZ and ANZ conformed to the proposed model.

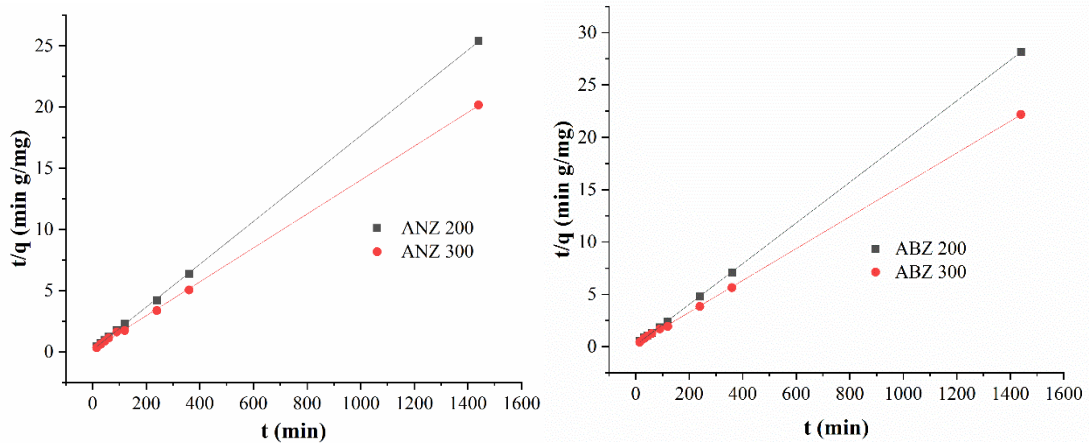

Fig. 8. Kinetic adsorption curves for silver adsorption onto (a) ANZ and (b) ABZ using a pseudo-second-order kinetics model

T a b l e 3

Kinetic parameters for Ag^+ removal on ANZ

Adsorbent ANZ	**Ag 200**	**Ag 300**
$q_{eq,\,exp}$ [mg/g]	56.70 ± 0.51	71.40 ± 1.25
Pseudo-first-order model		
$q_{eq,\,cal}$ [mg/g]	55.78 ± 0.84	74.54 ± 0.99
k_1 [1/min]	9.95 ± 0.25	28.25 ± 0.36
R^2	0.9087 ± 0.0650	0.8036 ± 0.0501
Pseudo-second-order model		
$q_{eq,\,cal}$ [mg/g]	57.52 ± 0.52	73.17 ± 1.02
κ_2 [g/mg min^{-1}]	0.0545 ± 0.0040	0.0251 ± 0.0010
R^2	0.9998 ± 0.0001	0.9989 ± 0.0004
Weber-Morris diffusion model		
K_{id1} [mg/g min$^{-1/2}$]	1.0662 ± 0.0320	1.8833 ± 0.2220
C_1 [mg/g]	10.8692 ± 0.2104	8.9812 ± 0.8410
R^2	0.955 ± 0.022	0.9830 ± 0.0230
K_{id2} [mg/g min$^{-1/2}$]	1.1245 ± 0.0121	0.0355 ± 0.0010
C_2 [mg/g]	39.5324 ± 0.4567	72.1516 ± 0.7800
R^2	0.9956 ± 0.0203	0.9995 ± 0.0010
K_{id3} [mg/g min$^{-1/2}$]	0.0658 ± 0.0010	
C_3 [mg/g]	58.5664 ± 1.2500	
R^2	0.9619 ± 0.0150	

T a b l e 4

Kinetic parameters for Ag^+ removal on ABZ

Adsorbent ABZ	**Ag 200**	**Ag 300**
$q_{eq,\,exp}$ [mg/g]	51.10 ± 0.51	64.90 ± 1.05
Pseudo-first-order model		
$q_{eq,cal}$ [mg/g]	52.49 ± 0.84	62.13 ± 0.99
k_1 [1/min]	7.95 ± 0.25	34.20 ± 0.36
R^2	0.8757 ± 0.0820	0.8073 ± 0.0510
Pseudo-second-order model		
$q_{eq,cal}$ [mg/g]	52.52 ± 0.52	65.07 ± 1.02
κ_2 [g/mg min^{-1}]	0.0545 ± 0.0041	0.0251 ± 0.0010
R^2	0.9988 ± 0.0001	0.9974 ± 0.0021
Weber-Morris diffusion model		
K_{id1} [mg/g min$^{-1/2}$]	2.0232 ± 0.0320	1.8833 ± 0.2210
C_1 [mg/g]	22.8902 ± 0.0153	8.9812 ± 0.8400
R^2	0.9928 ± 0.0221	0.9830 ± 0.0230
K_{id2} [mg/g min$^{-1/2}$]	0.0958 ± 0.0010	0.0355 ± 0.0010
C_2 [mg/g]	59.8764 ± 1.2510	65.1516 ± 0.98
R^2	0.9119 ± 0.0235	0.9995 ± 0.0010
K_{id3} [mg/g min$^{-1/2}$]	4.2558 ± 0.0010	
C_3 [mg/g]	19.87764 ± 1.2510	
R^2	0.9838 ± 0.0235	

Moreover, the calculated adsorption capacities at equilibrium, derived from the pseudo-second-order model, were in accordance with the experimentally obtained values (q_{eq}, exp) (see Tables 3 and 4). Based on these results, it was concluded that the adsorption of Ag^+ onto ANZ and ABZ followed a pseudo-second-order model. The adsorption process involved ion exchange and the

interaction of Ag^+ with amino groups in APTES molecules present on the zeolite surface. These findings were consistent with the ion exchange study (Table 2).

Furthermore, the Weber-Morris intraparticle diffusion model was employed to explore the influence of intraparticle diffusion on the removal processes (see Fig. 9). The presence of split linear zones in Figure 9 indicated that intraparticle diffusion was not the sole rate-determining step; instead, multiple mechanisms contributed to the adsorption of the tested ions. The intraparticle diffusion data for Ag^+ adsorption clearly indicated that the adsorption mechanism varied with initial concentration.

For ANZ at 200 mg/l, the plot exhibited three distinct linear regions, suggesting the involvement of multiple steps in the overall sorption process. These regions corresponded to: (i) external surface diffusion (boundary layer diffusion) of Ag^+ ions from the bulk solution to the adsorbent surface; (ii) intraparticle diffusion of ions into the pores of the adsorbent; and (iii) a final equilibrium phase, where the adsorption rate significantly slowed due to site saturation. This triphasic behavior reflected the classical intraparticle diffusion model described by Simić et al.[53] for Cd^{2+} biosorption, in which similar multistep diffusion processes were observed depending on the nature and structure of the adsorbent.

In contrast, for the adsorption at 300 mg/l, only two distinct linear segments were observed. The absence of a clearly defined third phase suggested that the equilibrium was reached more rapidly at a higher concentration, likely due to the increased driving force for mass transfer and enhanced diffusion. At this concentration, external diffusion and intraparticle transport dominated, while the equilibrium stage appeared less distinguishable.

Although the presence of multiple linear regions in the Weber-Morris plots indicated that more than one mass transfer step is involved, the steep initial slopes and high correlation with the pseudo-second-order model suggested that film diffusion and surface chemisorption were the predominant mechanisms governing Ag^+ adsorption onto ANZ and ABZ.

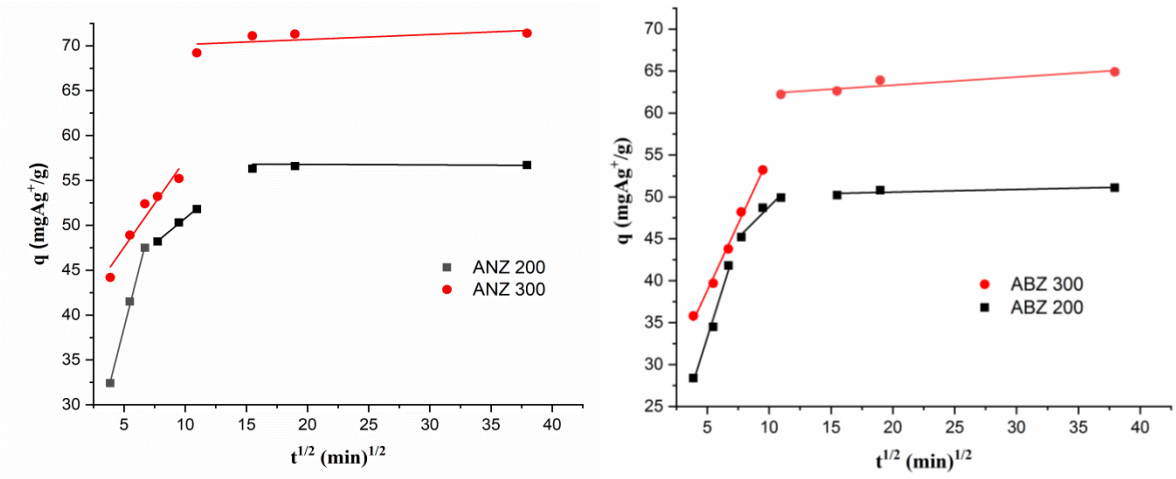

Fig. 9. Intraparticle diffusion plots of silver ions onto ANZ and ABZ

3.5. *Isotherm study*

To examine the silver adsorption equilibrium on ANZ and ABZ, the experimental data were fitted to Langmuir, Freundlich, and Temkin isotherm models. These isotherms served as valuable tools for understanding the interaction mechanisms between the metal ions and adsorbent materials, thereby providing insights into the binding mechanisms.[54]

The Langmuir model, which describes single-layer adsorption on a fixed number of active sites, is represented by Equation (5):[55]

$$q_e = q_{max} K_L C_e / (1 + K_L C_e) \quad (5)$$

where C_e (mg/l) is the equilibrium concentration, q_{max} denotes the maximum adsorption capacity (mg/g), and K_L is the Langmuir constant (l/mg). The feasibility and suitability of silver adsorption were further assessed using the dimensionless separation factor (R_L), as defined by Equation (6):[56]

$$R_L = 1/(1 + K_L C_0) \quad (6)$$

where C_0 represents the initial concentration of silver ions in solution (mg/l), R_L indicates the nature of the

adsorption process on ANZ and ABZ. A value of $R_L > 1$ suggests unfavorable adsorption, $R_L = 1$ indicates linearity, $0 < R_L < 1$ implies favorable adsorption and $R_L = 0$ signifies irreversible adsorption.[57]

The Freundlich isotherm, which describes multilayer adsorption on a heterogeneous surface, is represented by Equation (7):[58]

$$q_e = K_F C_e^{1/n} \quad (7)$$

where K_F (mg/g (mg/l)$^{-1/n}$) is the Freundlich constant, and *1/n* is the constant related to the material heterogeneity. A value of *n* between 1 and 10 suggests a specific adsorption process.

The Temkin isotherm, which considers adsorbent–adsorbate interactions and assumes that the heat of adsorption decreases linearly with coverage, is expressed by Equation (8):[59]

$$q_e = BLn\,KT + BLnCe \quad (8)$$

where $B = RT/b$ (J/mol) is a constant related to the heat of adsorption, K_T (L/g) is the Temkin equilibrium binding constant, R is the universal gas constant (8.314 J/mol·K), and T is the absolute temperature (K). The linear reduction in adsorption energy reflects a uniform distribution of binding energies up to some maximum value. The magnitude of B provides insight into the nature of adsorption: values below 40 kJ/mol typically indicate physisorption, while higher values suggest chemisorption.

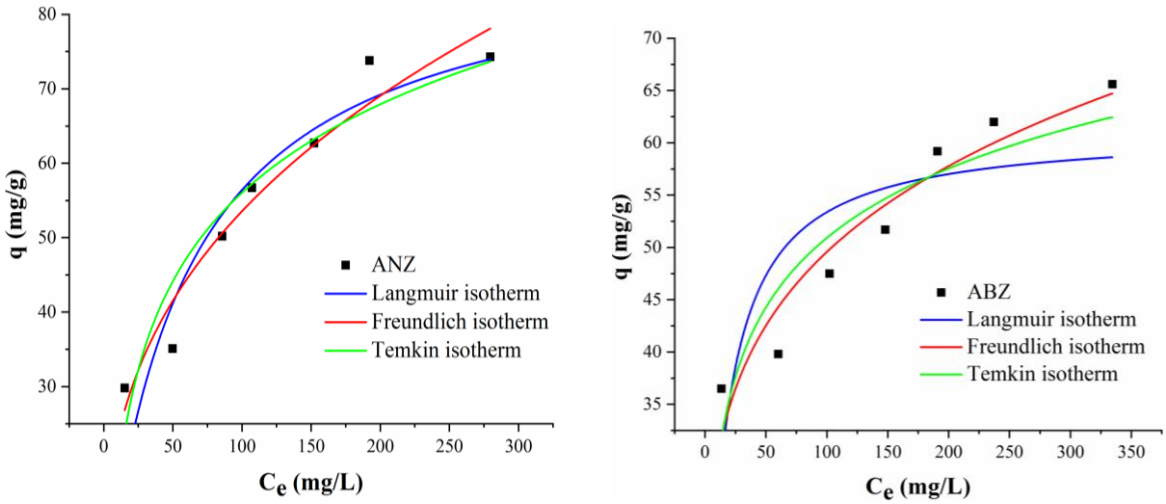

Fig. 10. Non-linear fits to different isotherm models of the Ag^+ adsorption by ABZ and ANZ

The equilibrium data were subjected to fitting procedures using the isotherm models, while the coefficient of determination (R^2) served as the primary criterion for model selection. Fig. 10 illustrated the inherent models depicting Ag^+ ion adsorption isotherms on ANZ and ABZ, while Table 5 delineated the derived parameters.

Analysis of the tabulated results indicated that the Freundlich equation provided a practical depiction of the experimental dataset, suggesting the occurrence of multilayer adsorption on the heterogeneous surfaces of ANZ and ABZ. Furthermore, ANZ demonstrated superior adherence to the Freundlich model – a trend consistent with the material characterization findings obtained through experimental methods.

In addition, the values of R_L and *1/n* ranged between 0 – 1 and 0 – 10, respectively, indicating favorable adsorption of Ag^+ ions onto ANZ and ABZ. Moreover, the favorable adsorption of silver on the examined ANZ and ABZ (primarily on ANZ) was confirmed by other calculated parameters summarized in Table 5. These parameters supported the claim, as $K_L < 1$, $K_F > 1$, and n_s values fell within the range of 0 to 1. According to calculated values, the maximum adsorption capacities of Ag^+ on ANZ and ABZ are 89.49 and 61.19 mg/g, respectively.

In addition to the Langmuir and Freundlich models, the Temkin isotherm was applied to gain further insight into the adsorption mechanism. This model assumed that the adsorption heat of all molecules in the layer decreased linearly with coverage due to adsorbent–adsorbate interactions. The Temkin model showed a good fit to the experimental data for both ANZ ($R^2 = 0.9064$) and ABZ ($R^2 = 0.8580$), suggesting its applicability.

T a b l e 5

Parameters and determination coefficients of the isotherm models

Models	Parameters	ANZ	ABZ
Langmuir	q_m (mg/g)	89.49 ± 3.15	61.19 ± 4.28
	K_L (l/mg)	0.020 ± 0.001	0.060 ± 0.001
	R^2	0.8947 ± 0.0021	0.6490 ± 0.0013
	R_L	0.010 ± 0.001	0.42 ± 0.02
	χ^2	9.44 ± 0.08	14.79 ± 0.04
Freundlich	K_F(mg/g)(l/mg)$^{1/n}$	9.88 ± 1.18	17.92 ± 0.45
	1/n	2.83 ± 1.02	4.74 ± 0.15
	R^2	0.9559 ± 0.0127	0.9171 ± 0.0098
	χ^2	14.48 ± 1.89	12.77 ± 0.98
Temkin	B (mg/g)	17.14 ± 2.14	9.57 ± 1.74
	K_T (l/mg)	0.263 ± 0.130	2.041 ± 0.947
	R^2	0.9064 ± 0.0134	0.8580 ± 0.0102

The calculated Temkin constant *B*, which was related to the heat of adsorption, was 17.14 mg/g for ANZ and 9.57 mg/g for ABZ. Since *B* values lower than 20 kJ/mol typically indicated physisorption, while values above this threshold pointed toward chemisorption, the obtained *B* values suggested that the adsorption of Ag^+ onto both ANZ and ABZ proceeded predominantly via physical interactions.

Additionally, the relatively low K_T values (0.263 l/mg for ANZ and 2.04 l/mg for ABZ) supported this conclusion, indicating a moderate binding strength between the adsorbent and Ag^+ ions.

3.6. *Antibacterial activity*

To investigate the potential application of the prepared samples, we examined the use of silane-modified, silver-enriched ANZ and ABZ as antibacterial agents. The antibacterial activity of the zeolites was tested toward two bacterial strains: *Escherichia coli* DSM 498, a representative of Gram-negative bacteria, and *Staphylococcus aureus* ATCC 25923, a representative of Gram-positive bacterial species.

The graphical representation in Figure 11 illustrated the absence of antibacterial activity exhibited by the APTES-modified zeolite against *Escherichia coli*. Conversely, a low antibacterial effect was observed when ABZ was tested against *Staphylococcus aureus*, as shown in Figure 12. Zones of inhibition were present when the antibacterial activity of Ag-enriched zeolites was examined against both strains (Figs. 11 and 12). This effect was attributed to the slow release of the Ag^+ ions from the zeolite lattice.

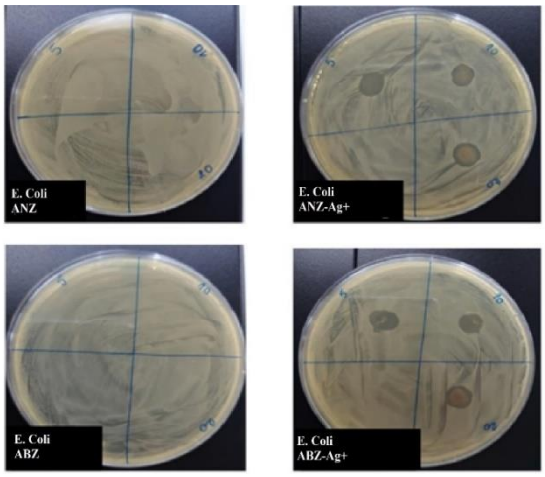

Fig. 11. Antibacterial activity of silane-modified, silver-enriched natural and beta zeolite against *Escherichia coli* DSM 498. Initial number of bacteria (t_0): *E. coli* DSM 498 = 1.2×10^9 CFU/cm^3

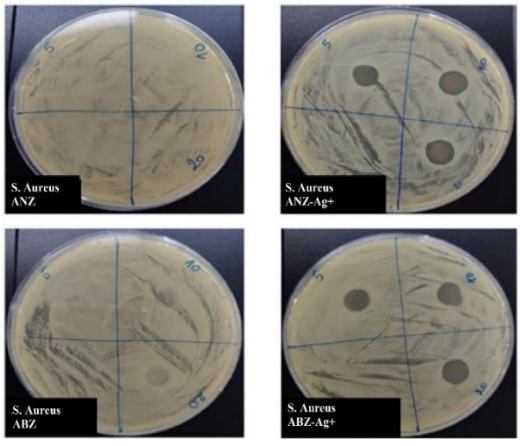

Fig. 12. Antibacterial activity of silane-modified, silver-enriched natural and beta zeolite against *Staphylococcus aureus* ATCC 25923. Initial number of bacteria (t_0): *S. aureus* ATCC 25923 = 2.4×10^8 CFU/cm^3

The zone of inhibition was more pronounced in the investigation of antibacterial activity against *S. aureus*, which could be explained by the structural difference between Gram-negative and Gram-positive bacteria. The cell wall of Gram-negative bacteria was more complex than gram-positive bacteria. Gram-negative bacteria contained a cell wall consisting of a thin peptidoglycan layer adjacent to the cytoplasmic membrane and an outer membrane (OM) composed of phospholipids and lipopolysaccharides, whereas the cell wall of gram-positive bacteria was thicker.[60]

This study showed that gram-positive *S. aureus* was more sensitive than gram-negative *E. coli*, and that the OM played a protective role against silver ions. Additionally, the inhibition zones for both bacteria increased with higher concentration of zeolite in the matrix, indicating concentration-dependent antibacterial activity.

4. CONCLUSIONS

This study investigated the feasibility of sequestering silver ions from aqueous solutions through the use of organically modified NZ and BZ. It focused particularly on their potential application as antimicrobial agents against pathogenic bacteria, specifically the gram-negative *Escherichia coli* and the gram-positive *Staphylococcus aureus*. Modification was achieved using APTES.

The results of infrared spectroscopy and thermogravimetric analysis corroborated the successful binding of the organic moiety to the zeolite matrix. Furthermore, the observed reduction in the specific surface area of both zeolites suggested that APTES binding occurred predominantly on the surface of the zeolite.

Analysis of the adsorption properties revealed a notable discrepancy in silver binding efficiency, with silane-modified NZ exhibiting significantly higher performance (86.7 %) compared to its beta zeolite counterpart (67.1 %) when exposed to a solution of identical initial concentrations (200 mg/dm^3). This performance difference was attributed to the higher concentration of exchangeable cations inherent in the structure of NZ, which facilitated both the binding of silver ions to APTES molecules and the ion exchange processes.

Subsequent evaluation of antibacterial activity confirmed the bactericidal efficacy of silver-saturated zeolites against both tested bacterial strains. This antimicrobial effect was attributed to the presence of silver ions, strategically positioned on the surface and within the structural framework of the zeolite.

***Acknowledgments*:** This work was supported by the Ministry of Science, Technological. Development and Innovation of the Republic of Serbia (Contract No. 451-03-136/2025-03/200023, 451-03-136/2025-03/200135, and 451-03-136/2025-03/200287).

REFERENCES

(1) Luan, H.; Xu, C.; Wu, Q.; Xiao, F. S., Recent advances in the synthesis of TS-1 zeolite, *Sec. Catalytic Reactions and Chemistry* **2022**, *10*. https://doi.org/10.3389%2Ffchem.2022.1080554

(2) Ugrina, M.; Gaberšek, M.; Daković, A.; Nuić, I., Preparation and characterization of the sulfur-impregnated natural zeolite clinoptilolite for Hg(II) removal from aqueous solutions, *Processes* **2021**, *9* (2), 217. https://doi.org/10.3390/pr9020217

(3) Rajić, N.; Stojaković, Dj.; Jevtić, S.; Zabukovec Logar, N.; Kovač, J.; Kaučić, V., Removal of aqueous manganese using the natural zeolitic tuff from the Vranjska Banja deposit in Serbia, *Journal of Hazardous Materials* **2009**, *172* (2–3), 1450–1457. https://doi.org/10.1016/j.jhazmat.2009.08.011

(4) Rakić-Milojević, M.; Bogdanović-Bajuk, D., Recent advances in zeolites and porous materials applications in catalysis and adsorption processes, *Catalysts* **2023**, *13* (5), 863. https://doi.org/10.3390/catal13050863

(5) Jevtić, S.; Arčon, I.; Rečnik, A.; Babić, B.; Mazaj, M.; Pavlović, J.; Matijašević, D.; Nikšić, M.; Rajić, N., The iron(III)-modified natural zeolitic tuff as an adsorbent and carrier for selenium oxyanions, *Microporous and Mesoporous Materials* **2014**, *197*, 92–100. https://doi.org/10.1016/j.micromeso.2014.06.008

(6) Weckhuysen, B. M.; Yu, J., Recent advances in zeolite chemistry and catalysis, *Chemical Society Reviews*, **2015**, Issue 20. https://doi.org/10.1039/C5CS90100F

(7) Santos da Silva, A.; Novais da Rocha, Z.; Mignoni, M. L., Z. dos Santos, J. H., Solvent-free synthesis of modified zeolites using hybrid silicas as raw material, *Microporous and Mesoporous Materials* **2019**, *290*, 109684. https://doi.org/10.1016/j.micromeso.2019.109684

(8) Brazovskaya, E. Yu.; Golubeva, O. Yu., Study of the effect of isomorphic substitutions in the framework of zeolites with a beta structure on their porosity and sorption characteristics, *Glass Physics and Chemistry* **2017**, *43*, 357–362. https://doi.org/10.1134/S1087659617040046

(9) Pasti, L.; Sarti, E.; Cavazzini, A.; Marchetti, N.; Dondi, F.; Martucci, A., Factors affecting drug adsorption on beta zeolite, *Journal of Separation Science* **2013**, *36*, (9–10) 1604-161. https://doi.org/10.1002/jssc.201201142

(10) Kuldeyev, E.; Seitzhanova, M.; Sandugash Tanirbergenova, S.; Tazhu, K.; Doszhanov, E.; Mansurov, Z.; Azat, S.; Nurlybaev, R.; Berndtsson, R.; Modifying natural zeolites to improve heavy metal adsorption, *Water* **2023**, *15* (12), 2215. https://doi.org/10.3390/w15122215

(11) Souza, I. M. S. Borrego-Sánchez, A.; Rigoti, E.; Sainz-Díaz, C. I.; Viseras, C.; Pergher, S. B. C., Experimental

and molecular modelling study of beta zeolite as drug delivery system, *Microporous and Mesoporous Materials* **2021**, 321, 111152. https://doi.org/10.1016/j.micromeso.2021.111152

(12) Miao, C.; Wang, L.; Zhou, S.; Yu, D.; Zhang, C.; Gao, S.; Yu, X.; Zhao, Z., Preparation of mesoporous zeolites and their applications in catalytic elimination of atmospheric pollutants, *Catalysts* **2024**, *14* (1), 75. https://doi.org/10.3390/catal14010075

(13) Shirendev, N.; Bat-Amgalan, M.; Kano, N.; Kim, H. J.; Gunchin, B.; Ganbat, B.; Yunden, G., A natural zeolite developed with 3-aminopropyltriethoxysilane and adsorption of Cu(II) from aqueous media, *Appleid Science* **2022**, *12* (22), 11344. https://doi.org/10.3390/app122211344

(14) Buffet-Bataillon, S.; Tattevin, P.; Bonnaure-Mallet, M.; Jolivet-Gougeon, A., Emergence of resistance to antibacterial agents: the role of quaternary ammonium compounds – a critical review, *Int. J. Antimicrob. Agents* **2012**, *39* 381–389. http://dx.doi.org/10.1016/j.ijantimicag.2012.01.011

(15) Senila, M.; Cadar,O.; Modification of natural zeolites and their applications for heavy metal removal from polluted environments: Challenges, recent advances, and perspectives, *Heliony* **2024**, *10* (3), e25303. https://doi.org/10.1016/j.heliyon.2024.e25303

(16) Han, X.; Yu, J.; Cao, Z.; Wang, R.; Du, W.; He, P.; Ge, Y., Preparation and properties of silane coupling agent modified zeolite as warm mix additive, *Construction and Building Materials* **2020**, *244*, 118408. https://doi.org/10.1016/j.conbuildmat.2020.118408

(17) Popaliya, M.; Mishra, A., Modified zeolite as an adsorbent for dyes, drugs, and heavy metal removal: a review, *International Journal of Environmental Science and Technology* **2023**, *20*, 12919–12936. http://dx.doi.org/10.1007/s13762-022-04603-z

(18) Madden, D., Curtin, T., Carbon dioxide capture with amino-functionalised zeolite-b: A temperature programmed desorption study under dry and humid conditions, *Microporous and Mesoporous Materials* **2016**, *228*, 310–317. https://doi.org/10.1016/j.micromeso.2016.03.041

(19) Zhu, Z., Xu, H., Jiang, J., Wu, H., Wu, P., Hydrophobic nanosized all-silica beta zeolite: efficient synthesis and adsorption application, *ACS Appl. Mater. Interfaces* **2017**, *9* (32), 27273–27283. https://doi.org/10.1021/acsami.7b06173

(20) Pasti, L.; Sarti, E.; Cavazzini, A.; Marchetti, N.; Dondi, F.; Martucci, A., Factors affecting drug adsorption on beta zeolites, *Separation science* **2013**, *36* (9–10), 1604-1611. https://doi.org/10.1002/jssc.201201142

(21) Saint-Cricq, P.; Kamimura, Y.; Itabashi, K.; Sugawara-Narutaki, A.; Shimojima, A.; Okubo, T., Antibacterial activity of silver-loaded "green zeolite", *European Journal of Inorganic Chemistry* **2012**, *21*, 3398–3402. https://doi.org/10.1002/ejic.201200476

(22) Dallas, P.; Sharma, V. K.; Zboril, R., Silver polymeric nanocomposites as advanced antimicrobial agents: classification, synthetic paths, applications, and perspectives, *Adv. Colloid Interface Sci.* **2011**, *166*, 119–135. http://dx.doi.org/10.1016/j.cis.2011.05.008

(23) Han, X.; Zhilong Cao a; Wang, R.; He, P.; Zhang, Y.; Yu, J.; Ge, Y., Effect of silane coupling agent modified zeolite warm mix additives on properties of asphalt, *Construction and Building Materials* **2020**, *259*, 119713. https://doi.org/10.1016/j.conbuildmat.2020.119713

(24) Jelić, A.; Sekulić, M.; Travica, M.; Gržetić, J.; Ugrinović, V.; Marinković, A. D.; Božić, A.; Stamenović, M.; Putić, S., Determination of mechanical properties of epoxy composite materials reinforced with silicate nanofillers using digital image correlation (DIC), *Polymers* **2022**, *14* (6), 1255. https://doi.org/10.3390/polym14061255

(25) Özel, C.; Akat, C.; R. Alosmanov, A.; Kahveci, M. U.; Emir, C.; Yücel, S.; Surface modification of zeolite and kaolin with 3-(aminopropyl) triethoxysilane and 3-(trimethoxysilyl) propyl methacrylate. *Bulgarian Chemical Communications* **2021**, *53* (4), 464–470. DOI: 10.34049/bcc.53.4.T003464

(26) Veličković, Z. S.; Vuković, G. D.; Marinković, A. D.; Moldovan, M. S.; Perić-Grujić, A. A.; Uskoković, P. S.; Ristić, M. D., Adsorption of arsenate on iron(III) oxide coated ethylenediamine functionalized multiwall carbon nanotubes, *Chem. Eng. J.* 2012, *181–182*, 174–181. https://doi.org/10.1016/j.cej.2011.11.052

(27) Miloševića, D. L.; Tomić, N. Z., Đokić, V. R.; Vidovića, M. M.; Veličković, Z. S., Jančić-Heinemann, R., Marinković, A. D., Structural and surface modification of highly ordered alumina for enhanced removal of Pb^{2+}, Cd^{2+} and Ni^{2+} from aqueous solution, *Desalination and Water Treatment* **2020**, *178*, 220–239. https://doi.org/10.5004/dwt.2020.24982

(28) Hudzicki, J., *Kirby-Bauer Disk Diffusion Susceptibility*. Test Protocol, **2009**. Corpus ID: 125831583

(29) Dong, Y.; Lin, H.; He, Y., Correlation between physicochemical properties of modified clinoptilolite and its performance in the removal of ammonia-nitrogen, *Environmental Monitoring and Assessment* **2017**, *189*, 107. https://doi.org/10.1007/s10661-017-5806-9

(30) Ortegon, D.; Rojas, J.; Meza, J.; Diaz, E.; Roa, M.; Characterization of the clinoptilolite zeolite and its potential application as the basis of a filtering system for the oil industry, *Journal of Physics: Conference Series* **2021**, *2046*, 012044. DOI:10.1088/1742-6596/2046/1/012044

(31) *Collection of Simulated XRD Powder Patterns for Zeolites*, Editors: M. M. J. Treacy and J. B. Higgins. Elsevier 2001. ISBN: 9780080529349

(32) Sher, A., Characterization of beta zeolites by X-ray diffraction, scanning electron microscope, and refractive index techniques, *Journal of the Chemical Society of Pakistan* **2010**, *32* (5), 592–598.

(33) Kukobat, R.; Škrbić, R.; Massiani, P.; Baghdad, K.; Launay, F.; Sarno, M.; Cirillo, C.; Senadore, A.; Salcin, E.; Atlagić, S. G., Thermal and structural stability of microporous natural clinoptilolite zeolite, *Microporous and Mesoporous Materials* 2022, *341*, 112101. https://doi.org/10.1016/j.micromeso.2022.112101

(34) Mitchell, S.; Bonilla, A.; Pérez-Ramírez, J., Preparation of organic-functionalized mesoporous ZSM-5 zeolites by consecutive desilication and silanization, *Materials*

Chemistry and Physics **2011**, *127* (1–2), 278–284. https://doi.org/10.1016/j.matchemphys.2011.02.003

(35) Zendelska, A.; Golomeova, M.; Jakupi, Š.; Kuvendziev, S.; Lisichkov, K.; Marinkovski, M., Characterization and application of clinoptilolite for removal of heavy metal ions from water resources, *Geologica Macedonica* **2018**, *32* (1), 21–32.

(36) Akata, B.; Yilmaz, B.; Jirapongphan, S. S.; Warzywoda, J.; Sacco Jr, A., Characterization of zeolite Beta grown in microgravity, *Microporous and Mesoporous Materials* **2004**, *71* (1–3), 1–9. https://doi.org/10.1016/j.micromeso.2004.03.012

(37) Chen, T.; Gu, C.; Ouyang, Y.; Zhuang, L.; Yao, Z.; Zou, K.; Wang, Y.; Luo, Y.; Shu, X., Synthesis of high hydrothermal stability Beta zeolite with crosslinked starch and catalytic performance in catalytic cracking reaction, *Fuel* **2022**, *318*, 123696. https://doi.org/10.1016/j.fuel.2022.123696

(38) Bayat, M.; Javanbakht, V.; Esmai, J., Synthesis of zeolite/nickel ferrite/sodium alginate bionanocomposite via a co-precipitation technique for efficient removal of water-soluble methylene blue dye, *International Journal of Biological Macromolecules* **2018**, *116*, 607–619. https://doi.org/10.1016/j.ijbiomac.2018.05.012

(39) Moradmard, H.; Shayesteh, S. F.; Tohidi, P.; Abbas, Z.; Khaleghi, M., Structural, magnetic and dielectric properties of magnesium doped nickel ferrite nanoparticles, *Journal of Alloys and Compounds* **2015**, *650*, 116–122.

(40) Daemi, H.; Barikani, M.; Barmar, M., Variations in calcium and alginate ions concentration in relation to the properties of calcium alginate nanoparticles, *Science and Technology* **2013**, *26* (1), 25–32.

(41) Holub, M., Balintova, M., Demcak, S., Hurakova, M., Characterization of natural zeolite and determination its adsorption properties, *Journal of Civil Engineering, Environment and Architecturs*, **2016**. DOI:10.7862/rb.2016.192

(42) Breck, D. W., Zeolite molecular sieves: structure, chemistry, and use. *Wiley-Interscience Journal of Chromatographic Science* **1975**, *13* (4), 18A. https://doi.org/10.1093/chromsci/13.4.18A-c

(43) Mintova, S.; Gilson, J. P.; Valtchev, V., Advances in the nanoscale engineering of zeolites for applications in catalysis and adsorption. *Chemical Society Reviews* **2013**, *42* (9), 3690–3707. https://doi.org/10.1039/C3CS35457C

(44) Cundy, C. S.; Cox, P. A., The hydrothermal synthesis of zeolites: history and development from the earliest days to the present time. *Chemical Reviews* **2003**, *103* (3), 663–701. https://doi.org/10.1021/cr020060i

(45) Jevtić, S., Dimitrijević, J., Petrović, J., Dikić, J., Antibacterial activity of surface amine-functionalized silver-enriched zeolite , XIV *Conference of chemists, technologists and environmentalists of Republic of Srpska*, 2022, 178–178 Banja Luka: University in Banja Luka, Faculty of Technology.

(46) Petrović, J.; Stojanović, M.; Milojković, J.; Petrović, M.; Šoštarić, T.; Laušević, M.; Mihajlović, L. M., Alkali modified hydrochar of grape pomace as a perspective adsorbent of Pb^{2+} from aqueous solution, *Journal of Environmental Management* **2016**, *182*, 292–300. https://doi.org/10.1016/j.jenvman.2016.07.08119

(47) Dimitrijević, J.; Jevtić, S.; Marinković, A.; Simić, M.; Koprivica, M.; Petrović, J., Ability of deep eutectic solvent modified oat straw for Cu(II), Zn(II), and Se(IV) ions removal. *Processes* **2023**, *11*. https://doi.org/10.3390/pr11051308

(48) Abdellaoui, Y.; El Ibrahimi, B.; Ahrouch, M.; Zineb Kassab, Z.; Billah, R. E. K.; Coppel, Y.; López-Maldonado, E. A.; Oualid, A. O.; Díaz de León, J. N.; Leiviskä, T.; Giácoman-Vallejos, G.; Gamero-Melo, P., New hybrid adsorbent based on APTES functionalized zeolite W for lead and cadmium ions removal: Experimental and theoretical studies, *Chemical Engineering Journal* **2024**, *499*, 156056. https://doi.org/10.1016/j.cej.2024.156056

(49) Velarde, L.; Nabavi, S. M.; Escalera, E.; Antti, L. M.; Akhtar, F., Adsorption of heavy metals on natural zeolites: A review, *Chemosphere* **2023**, *328*, 138508. https://doi.org/10.1016/j.chemosphere.2023.138508

(50) Lagergren, S., Zur Theorie der sogenannten Adsorption gelöster Stoffe, K. Sven. *Vetenskapsakad. Handl*. **1898**; *24*, pp. 1–39. https://doi.org/10.1007/BF01501332

(51) Ho, Y. S.; McKay, G., Pseudo-second order model for sorption processes, *Process Biochem*. **1999**, *34*, 451–465. https://doi.org/10.1016/S0032-9592(98)00112-5

(52) Weber, W.; Morris, J., Kinetics of adsorption on carbon from solution, *J. Sanit. Eng. Div*. **1963**, *89*, 31–60. https://doi.org/10.1061/JSEDAI.0000430

(53) Simić, M.; Petrović, J.; Šoštarić, T.; Ercegović, M.; Milojković, J.; Lopičić, Z.; Kojić, M., A mechanism assessment and differences of cadmium adsorption on raw and alkali-modified agricultural waste, *Processes* **2022**, *10* (10), 1957. https://doi.org/10.3390/pr10101957

(54) Petrović, J.; Ercegović, M.; Simić, M.; Kalderis, D.; Koprivica, M.; Milojović, J.; Radulović, D.; Novel Mg-doped pyro-hydrochars as methylene blue adsorbents: Adsorption behavior and mechanism, *Journal of Molecular Liquids* **2023**, *376*, 121424. https://doi.org/10.1016/j.molliq.2023.121424

(55) Langmuir, I., The adsorption of gases on plane surfaces of glass, mica and platinum, *J. Am. Chem. Soc*. **1918**, *40*, 1361–1403. https://doi.org/10.1021/ja02242a004

(56) Webber, T. W.; Chakkravorti, R. K., Pore and solid diffusion models for fixed-bed adsorbers, *AlChE J*. **1974**, *20*, 228–238. https://doi.org/10.1002/aic.690200204

(57) Foo, K. Y.; Hameed, B. H., Insights into the modeling of adsorption isotherm systems, *Chem. Eng. J*. **2010**, *156*, 2–10. https://doi.org/10.1016/j.cej.2009.09.013

(58) Freundlich, H. M. F., Über die Adsorption in Lösungen, *Z. Phys. Chem*. **1906**, *57* A, 385–470. https://doi.org/10.1515/zpch-1907-5723

(59) Temkin, M. I., and Pyzhev, V., Kinetic of ammonia synthesis on promoted iron catalyst, *Acta Phy. Chem*, URSS 12, 327-356, 1940.

(60) Slavin, Y. N.; Asnis, J.; Häfeli, U. O.; Bach, H., Metal nanoparticles: understanding the mechanisms behind antibacterial activity, *Journal of Nanobiotechnology* **2017**, *15*, 65. https://doi.org/10.1186/s12951-017-0308-z